Quantum mechanical calculation of the collision-induced absorption spectra of N_2–N_2 with anisotropic interactions

Tijs Karman, Evangelos Miliordos, Katharine L. C. Hunt, Gerrit C. Groenenboom, and Ad van der Avoird

Citation: The Journal of Chemical Physics **142**, 084306 (2015); doi: 10.1063/1.4907917
View online: http://dx.doi.org/10.1063/1.4907917
View Table of Contents: http://aip.scitation.org/toc/jcp/142/8
Published by the American Institute of Physics

Quantum mechanical calculation of the collision-induced absorption spectra of N_2–N_2 with anisotropic interactions

Tijs Karman,[1] Evangelos Miliordos,[2] Katharine L. C. Hunt,[2] Gerrit C. Groenenboom,[1] and Ad van der Avoird[1,a)]

[1]*Theoretical Chemistry, Institute for Molecules and Materials, Radboud University Nijmegen, Nijmegen, The Netherlands*

[2]*Department of Chemistry, Michigan State University, East Lansing, Michigan 48824, USA*

(Received 2 December 2014; accepted 30 January 2015; published online 25 February 2015)

We present quantum mechanical calculations of the collision-induced absorption spectra of nitrogen molecules, using *ab initio* dipole moment and potential energy surfaces. Collision-induced spectra are first calculated using the isotropic interaction approximation. Then, we improve upon these results by considering the full anisotropic interaction potential. We also develop the computationally less expensive coupled-states approximation for calculating collision-induced spectra and validate this approximation by comparing the results to numerically exact close-coupling calculations for low energies. Angular localization of the scattering wave functions due to anisotropic interactions affects the line strength at low energies by two orders of magnitude. The effect of anisotropy decreases at higher energy, which validates the isotropic interaction approximation as a high-temperature approximation for calculating collision-induced spectra. Agreement with experimental data is reasonable in the isotropic interaction approximation, and improves when the full anisotropic potential is considered. Calculated absorption coefficients are tabulated for application in atmospheric modeling. © *2015 AIP Publishing LLC.* [http://dx.doi.org/10.1063/1.4907917]

I. INTRODUCTION

Molecular nitrogen is the dominant component of the atmospheres of the Earth, Titan, and early Mars.[1] Collision-induced absorption due to N_2 pairs contributes significantly to the far infrared absorption spectra of these atmospheres. Therefore, accurate knowledge of the collision-induced spectra is required for remote-sensing studies.[2] Collisions with abundant N_2 molecules also lead to broadening of strong absorption lines,[3] such as the water continua in the Earth's atmosphere.[4] The far infrared absorption of N_2 pairs also contributes to surface warming,[5] and this mechanism may be essential in explaining the presence of liquid water on early Mars.[1]

Previous quantum mechanical calculations of the collision-induced rotation-translation absorption spectra of N_2–N_2 have been performed by Borysow and Frommhold.[6] In these calculations, effective isotropic potentials were used in combination with adjusted collision-induced dipole moments. Laboratory measurements of the collision-induced N_2–N_2 spectra have also been performed.[7–10] Boissoles *et al.* investigated the collision-induced absorption of N_2–N_2, N_2–O_2, and O_2–O_2, using empirical line-shapes.[11,12] First principles potential energy and dipole moment surfaces were used in classical molecular dynamics simulations of collision-induced spectra by Bussery-Honvault and Hartmann.[13] In contrast to what one would expect for a classical treatment, the agreement between the simulated and experimental spectra is better for lower temperatures.

In this paper, we present quantum mechanical calculations of the collision-induced N_2–N_2 spectra, using the theory presented in the companion paper[14] and first principles potential energy and dipole moment surfaces. We performed calculations using the isotropic interaction approximation, the coupled-states approximation, and the numerically exact close-coupling approach. The coupled-states approximation neglects weak Coriolis coupling, but takes the full anisotropy of the interaction into account. Results obtained in this approximation are close to the numerically exact calculations and approach the results obtained in the isotropic interaction approximation for high energy. At low energies, angular localization of the scattering wave function causes the line strength to differ from the result in the isotropic interaction approximation by several orders of magnitude. The effect of anisotropic interactions is to increase the band intensity, bringing the calculations into closer agreement with experimental data. For high energy, the effect of the anisotropy decreases, which validates the use of the isotropic interaction as a high-temperature approximation. However, in the isotropic interaction approximation, narrow shape resonances occur for high partial waves and energies, leading to unphysically sharp features in the spectrum that should be smoothed. To our knowledge, the present calculations are the first quantum mechanical calculations of collision-induced absorption including anisotropic interactions, except for nearly isotropic systems such as H_2–H_2 and H_2–He.[14–16]

This paper is organized as follows. The calculation of the potential energy and electric dipole moment surfaces is discussed in Sec. II. The line-shape theory is discussed in Sec. III. This includes a brief summary of the theory presented in the

a)Electronic address: avda@theochem.ru.nl

companion paper[14] in Sec. III A, a derivation of the coupled-states approximation to collision-induced spectra in Sec. III B, and a discussion of the contribution of the bound states in Sec. III C. The computational details are discussed in Sec. IV. Numerical results are presented and compared to experimental data in Sec. V and concluding remarks are given in Sec. VI.

II. ELECTRONIC STRUCTURE CALCULATIONS AND FIT

The calculation of collision-induced absorption spectra requires accurate potential energy and dipole moment surfaces. These are calculated using *ab initio* electronic structure theory, in calculations similar to those for the H_2–H_2 complex, described in Ref. 17. Here, we briefly describe the method that was used in these calculations and we discuss how these surfaces were fit.

Potential energy and dipole moment surfaces were obtained using the super-molecular approach. The method used is coupled-cluster theory with single and double excitations and perturbative triples [CCSD(T)], using an augmented correlation consistent quadruple zeta basis set (aug-cc-pVQZ). All calculations were corrected for the basis set superposition error.[18] The dipole moment was calculated from the linear response to a finite electric field, at the same level of theory. In four separate *ab initio* calculations for each geometrical configuration, uniform electric fields of ± 0.001 and $\pm 0.001\sqrt{2}$ a.u. were applied along the coordinate axes, and the results were analyzed to remove hyperpolarization effects through fourth order in the applied field. All calculations were performed for 29 orientations and 15 separations of the two molecules. The N_2 bond length was fixed at the vibrational average of 2.081 a_0.

For the T-shaped configuration, test calculations were run at intermolecular separations of 4.5, 7.0, and 15.0 a_0, with fields of ± 0.001, $\pm 0.001\sqrt{2}$, and $\pm 0.001\sqrt{3}$ a.u., in order to remove hyperpolarization effects through sixth order. The differences from the results obtained with four values of the applied field were less than 0.002% in these test cases. Calculations were also run with the larger aug-cc-pV5Z basis set, for the T-shaped configuration at the intermolecular distances listed above. In these test cases, after correcting for basis-set superposition errors, the largest difference between the results obtained with the aug-cc-pVQZ and aug-cc-pV5Z basis sets was less than 0.3%.

The potential energy surface was fit, in a linear least squares procedure, to the following expansion in coupled spherical harmonics:

$$V(\hat{r}_A, \hat{r}_B, \vec{R}) = \sum_{l_1,l_2,l} V_{l_1,l_2,l}(R) \times \left[\left[C^{(l_1)}(\hat{r}_A) \otimes C^{(l_2)}(\hat{r}_B)\right]^{(l)} \otimes C^{(l)}(\hat{R})\right]_0^{(0)}. \quad (1)$$

Similarly, the spherical components of the dipole operator, $\mu_0 = \mu_z$ and $\mu_{\pm 1} = \mp\left(\mu_x \pm i\mu_y\right)/\sqrt{2}$, were fit to the expansion

$$\mu_\nu(\hat{r}_A, \hat{r}_B, \vec{R}) = \sum_{l_1,l_2,l,\lambda} D_{l_1,l_2,l,\lambda}(R) \times \left[\left[C^{(l_1)}(\hat{r}_A) \otimes C^{(l_2)}(\hat{r}_B)\right]^{(l)} \otimes C^{(\lambda)}(\hat{R})\right]_\nu^{(1)}. \quad (2)$$

The irreducible spherical tensor product is defined by

$$\left[\hat{A}^{(l_1)} \otimes \hat{B}^{(l_2)}\right]_m^{(l)} = \sum_{m_1,m_2} \hat{A}_{m_1}^{(l_1)} \hat{B}_{m_2}^{(l_2)} \langle l_1 m_1 l_2 m_2 | l m \rangle, \quad (3)$$

the symbol in angular brackets denotes a Clebsch-Gordan coefficient, and $C_m^{(l)}(\hat{R})$ denotes a Racah normalized spherical harmonic depending on the polar angles of the vector $\vec{R} = R\hat{R}$, the vector that connects the centers of mass of both molecules. The vectors $\hat{r}_A$ and $\hat{r}_B$ denote the polar angles of the molecular axes of molecules A and B, respectively. The *ab initio* points and fitted expansion coefficients can be found in the supplementary material.[19]

To evaluate these expansions at arbitrary separation R, we performed a fit of the expansion coefficients, $V_{l_1,l_2,l}(R)$ and $D_{l_1,l_2,l,\lambda}(R)$. First, the long-range was fit to an expansion in powers of $1/R$, using an R^n weighted linear least squares fit, with n determined by the leading power of $1/R$. In the region $R \geq 12$ a_0, we fit the potential energy surface using terms with $n \leq 7$, whereas we fit the dipole surface using terms with $n \leq 6$ in the region $R \geq 15$ a_0. The long-range contributions were damped by multiplication with Tang-Toennies damping functions,[20]

$$f_{n,\beta}(R) = 1 - e^{-\beta R} \sum_{k=0}^{n} \frac{(\beta R)^k}{k!}, \quad (4)$$

where n is the corresponding power of $1/R$ and $\beta = 1.615\ a_0^{-1}$ is determined from the log-derivative of the isotropic potential in the repulsive region.[20] These damped long-range contributions were subtracted from the total to obtain the short-range part, which was fit for $R \leq 12$ using the reproducing Kernel Hilbert space method.[21] The smoothness parameter for this fit was set equal to two and the asymptotic behavior was chosen such that the short-range part falls off as the first term in the asymptotic expansion that was not fit explicitly in the long range.

III. LINE-SHAPE THEORY

A. Summary

To calculate collision-induced absorption spectra, we use the isotropic and anisotropic formalisms discussed in the companion paper.[14] The absorption coefficient is defined by Lambert's law, which predicts exponential decay of the intensity, $I(z) \propto \exp(-\alpha z)$, with the path length, z. In first order perturbation theory, the absorption coefficient at frequency ω is given by

$$\alpha(\omega, T) = \frac{2\pi^2}{3\hbar c} n^2 \omega \left[1 - \exp\left(-\frac{\hbar\omega}{k_B T}\right)\right] V g(\omega, T) \quad (5)$$

with the spectral density

$$g(\omega, T) = \sum_i \sum_f P^{(i)}(T) |\langle i|\hat{\boldsymbol{\mu}}|f\rangle|^2 \delta(\omega_f - \omega_i - \omega). \quad (6)$$

Here, n, V, and T are the number density, volume, and temperature of the gas, respectively, c is the speed of light, $\hbar$ is the reduced Planck constant, and $\hat{\boldsymbol{\mu}}$ represents the dipole operator. The states $|i\rangle$ and $|f\rangle$ represent the initial and final states, with energies $\hbar\omega_i$ and $\hbar\omega_f$, and $P^{(i)}(T)$ is the thermal population of

the initial state. The symbol $\sum\!\!\!\!\!\!\int$ denotes a summation over all discrete quantum numbers, such as rotational and vibrational states, and integration over the continuum, i.e., translational states.

The states $|i\rangle$ and $|f\rangle$ are the eigenstates of the Hamiltonian

$$\hat{H} = -\frac{\hbar^2}{2\mu}\nabla_R^2 + \hat{H}_A + \hat{H}_B + \hat{V}(\vec{r}_A, \vec{r}_B, \vec{R}), \tag{7}$$

that is, the Hamiltonian describing the molecular pair, but not the coupling with the radiation field. The first term represents the kinetic energy in the center of mass frame, $\hat{H}_A$ and $\hat{H}_B$ are the monomer Hamiltonians, and $\hat{V}(\vec{r}_A, \vec{r}_B, \vec{R})$ represents the interaction between the molecules. The eigenstates of this Hamiltonian can be divided in two distinct sets. A continuum of scattering states exists for positive energies, whereas the bound states correspond to a discrete set of eigenstates at negative energies. In the companion paper,[14] we did not consider the contribution of bound states to the collision-induced absorption spectra of H_2, as the weak interaction between two H_2 molecules supports only two weakly bound states. For N_2 pairs, the situation is markedly different,[6] as the isotropic potential now supports six rotationless bound states. In isotropic interaction calculations including the end-over-end rotation of the complex, 96 bound states are found per monomer rotational state. The contribution of these bound states is discussed in detail in Sec. III C.

The calculation of the absorption spectrum can be simplified by determining the eigenstates $|i\rangle$ and $|f\rangle$ in certain approximation schemes. We will start by assuming that the interaction between the two molecules, $\hat{V}$, is isotropic. In this approximation, the wave function describing the absorbing complex factorizes as the product of an angular wave function and a radial wave function.[14,22,23] The angular part of the wave function is known analytically, which allows one to explicitly perform part of the thermal averaging, required to obtain the absorption spectrum. Only the radial part must be determined numerically in a computationally inexpensive single-channel calculation. This separation of rotational and translational degrees of freedom allows one to write the spectral density as superposition of translational profiles centered at rotational transition frequencies given by $\hbar\omega_{\rm rot} = E'_{\rm rot} - E_{\rm rot}$,

$$\begin{aligned} Vg(\omega, T) = &\sum_{l_1,l_2,l,\lambda} \sum_{N_A,N_B,N'_A,N'_B} P_{N_A} P_{N_B} \\ &\times \frac{[1, N_A, N'_A, N_B, N'_B]}{[l_1, l_2, \lambda]} \\ &\times \begin{pmatrix} N_A & l_1 & N'_A \\ 0 & 0 & 0 \end{pmatrix}^2 \begin{pmatrix} N_B & l_2 & N'_B \\ 0 & 0 & 0 \end{pmatrix}^2 \\ &\times VG_{l_1,l_2,l,\lambda}(\omega - \omega_{\rm rot}), \end{aligned} \tag{8}$$

where the free-to-free contribution to the translational profile, VG, is given by

$$\begin{aligned} VG^{\rm free-free}_{l_1,l_2,l,\lambda}(\omega, T) = &\hbar\lambda_0^3 \sum_{L,L'} [L, L'] \begin{pmatrix} L & \lambda & L' \\ 0 & 0 & 0 \end{pmatrix}^2 \\ &\times \int_0^\infty dE_{\rm col} \exp\left(-\frac{E_{\rm col}}{k_B T}\right) \\ &\times |\langle E_{\rm col}, L | D_{l_1,l_2,l,\lambda} | E_{\rm col} + \hbar\omega, L' \rangle|^2, \end{aligned} \tag{9}$$

and contributions involving bound states are discussed in Sec. III C. In the above equations, the symbols in round braces are Wigner 3-jm symbols and we use the short-hand notation

$$[j_1, j_2, \ldots, j_n] = (2j_1 + 1)(2j_2 + 1)\ldots(2j_n + 1). \tag{10}$$

For a more realistic description, the orientation dependence of the interaction between the two nitrogen molecules should be considered. To take this anisotropy into account, we calculate the bound states of the anisotropic potential as described in Sec. III C and for the scattering states, we perform close-coupling calculations using the method described in Ref. 14. This method calculates the dipole coupling *on-the-fly*, which allows one to treat the absorption perturbatively rather than explicitly,[15,16] yet avoids the reconstruction of the full many-component wave function on a discrete radial grid. From a computational perspective, it is still prohibitive to calculate collision-induced spectra at temperatures of interest ($T \geq 78$ K) using the numerically exact close-coupling approach. The reason is that minimal basis sets including only the open channels at an energy of $E \approx 1000$ K already contain on the order of 30 000 channels. In Sec. III B, we therefore develop the coupled-states approximation for collision-induced spectra, which reduces the dimension of the channel basis for similar calculations to about 2000 channels.

B. Coupled-states approximation

In the companion paper,[14] we point out that the method developed to propagate the dipole coupling matrix may be used to introduce approximations for the computation of collision-induced spectra. In general, the strategy is to introduce approximations that block-diagonalize the coupling matrix, and use this block-diagonal structure to reduce the dimension of the basis set. In the case of the coupled-states approximation, we neglect off-diagonal Coriolis coupling by writing

$$\hat{L}^2 = \left(\hat{\boldsymbol{J}} - \hat{\boldsymbol{N}}\right)^2 = \hat{J}^2 + \hat{N}^2 - 2\hat{\boldsymbol{N}}\cdot\hat{\boldsymbol{J}} \approx \hat{J}^2 + \hat{N}^2 - 2\hat{N}_z\hat{J}_z, \tag{11}$$

where the angular momentum operator $\hat{\boldsymbol{L}}$ generates the end-over-end rotation of the complex, $\hat{\boldsymbol{J}}$ is the total angular momentum, and $\hat{\boldsymbol{N}} = \hat{\boldsymbol{N}}_A + \hat{\boldsymbol{N}}_B$, where $\hat{\boldsymbol{N}}_A$ and $\hat{\boldsymbol{N}}_B$ are the monomer angular momenta. In this *helicity-decoupling* approximation, the projection, K, of the total angular momentum onto the intermolecular axis is a good quantum number.[24] Hence, the calculation may be performed per K and K', the projection quantum numbers in the initial and final states, respectively.

To exploit the body-fixed projection, K, of the total angular momentum as a good quantum number, the calculation should be performed in a body-fixed frame. Here, the primitive angular basis functions are defined by[24]

$$\begin{aligned} &\langle \hat{R} | (N_A N_B) N K; J M \rangle \\ &\quad = \sum_{K_A,K_B} |N_A K_A\rangle |N_B K_B\rangle \\ &\qquad \times \langle N_A K_A N_B K_B | N K \rangle D^{(J)*}_{MK}(\phi, \theta, 0) \sqrt{\frac{2J+1}{4\pi}}, \end{aligned} \tag{12}$$

where (θ, ϕ) are the polar angles of the intermolecular axis $\vec{R}$, $D^{(J)}_{MK}$ is a Wigner D-matrix element, and the kets $|N_A K_A\rangle$ and $|N_B K_B\rangle$ describe the rotation of the monomers in the body-fixed frame. The matrix elements of the potential in this angular

basis are[24]

$$\begin{aligned}
&\langle (N_A N_B) NK; JM|\hat{V}|(N'_A N'_B) N'K'; J'M'\rangle \\
&\quad = \delta_{JJ'}\delta_{MM'}\delta_{KK'} \sum_{l_1,l_2,l} V_{l_1,l_2,l}(R)(-1)^{l+N_A+N_B+N-K} \\
&\qquad \times \left[N_A, N'_A, N_B, N'_B, N, N'\right]^{1/2} \\
&\qquad \times \begin{pmatrix} N_A & l_1 & N'_A \\ 0 & 0 & 0 \end{pmatrix} \begin{pmatrix} N_B & l_2 & N'_B \\ 0 & 0 & 0 \end{pmatrix} \\
&\qquad \times \begin{pmatrix} N & l & N' \\ -K & 0 & K' \end{pmatrix} \begin{Bmatrix} N_A & N'_A & l_1 \\ N_B & N'_B & l_2 \\ N & N' & l \end{Bmatrix}.
\end{aligned} \tag{13}$$

An additional advantage of the body-fixed frame is that this expression is simpler than the corresponding expression in the space-fixed basis, Eq. (A8) in Ref. 14. The matrix elements of the dipole moment are also simpler, they are given by[24]

$$\begin{aligned}
&\langle (N_A N_B) NK; JM|\hat{\mu}_\nu|(N'_A N'_B) N'K'; J'M'\rangle \\
&\quad = \sum_{k,l_1,l_2,l,\lambda} D_{l_1,l_2,l,\lambda}(R)(-1)^{N_A+N_B+N+M+l-\lambda+k} \\
&\qquad \times \left[1, l, N_A, N'_A, N_B, N'_B, N, N', J, J'\right]^{1/2} \\
&\qquad \times \begin{pmatrix} l & \lambda & 1 \\ k & 0 & -k \end{pmatrix} \begin{pmatrix} J & 1 & J' \\ -M & m & M' \end{pmatrix} \\
&\qquad \times \begin{pmatrix} J & 1 & J' \\ -K & k & K' \end{pmatrix} \begin{pmatrix} N & l & N' \\ -K & k & K' \end{pmatrix} \\
&\qquad \times \begin{pmatrix} N_A & l_1 & N'_A \\ 0 & 0 & 0 \end{pmatrix} \begin{pmatrix} N_B & l_2 & N'_B \\ 0 & 0 & 0 \end{pmatrix} \\
&\qquad \times \begin{Bmatrix} N_A & N'_A & l_1 \\ N_B & N'_B & l_2 \\ N & N' & l \end{Bmatrix}.
\end{aligned} \tag{14}$$

In the above equations, the symbols in curly braces are Wigner 9-j symbols. We note that, although the potential conserves the quantum numbers J, M, and K, the dipole moment couples states which differ in these quantum numbers by at most one unit.

Symmetry adapted functions are generated by acting on the primitive basis functions with projection operators $1 \pm \hat{E}^*$ and $1 \pm \hat{P}_{AB}$, in order to adapt to inversion, $\hat{E}^*$, and permutation, $\hat{P}_{AB}$, respectively. The action of these symmetry operators on the body-fixed angular functions is given by[24]

$$\begin{aligned}
&\hat{E}^*|(N_A N_B) NK; JM\rangle \\
&\quad = (-1)^{N_A+N_B-N+J}|(N_A N_B) N\ -K; JM\rangle, \\
&\hat{P}_{AB}|(N_A N_B) NK; JM\rangle \\
&\quad = (-1)^{N_A+N_B+J}|(N_B N_A) N\ -K; JM\rangle.
\end{aligned} \tag{15}$$

Since the channel functions of Eq. (12) do not have well-defined partial wave quantum numbers, L, we cannot match to the scattering boundary conditions in terms of the spherical Hankel functions, Eq. (34) of Ref. 14. Instead, we match the solutions to the asymptotic form of these functions given by

$$\begin{aligned}
h_L^{(1)}(kR) &\simeq -i(-1)^L \exp(ikR)(kR)^{-1}, \\
h_L^{(2)}(kR) &\simeq i(-1)^L \exp(-ikR)(kR)^{-1}.
\end{aligned} \tag{16}$$

The phase of the asymptotic form of the Hankel functions depends on whether L is even or odd, which can be determined from the parity of the wave function and $N_A + N_B$. In practice, this phase can be omitted as it does not affect the square of the dipole matrix elements that enter Eq. (6). The asymptotic form of the Hankel functions is valid when the centrifugal term vanishes, necessitating the propagation to larger intermolecular separation, R. We note that customarily, scattering calculations in the coupled-states approximation match the asymptotic form of the wave function to Hankel functions with some *effective* partial wave quantum number, L_{eff}, which is often taken equal to J.[25] This method should yield the same result, provided that we propagate to sufficiently large R, such that all Hankel functions approach their asymptotic form. Test calculations confirm that both approaches agree to within the selected convergence criterion of about 1%.

Often, the effective partial wave quantum number is not only used in the matching procedure but also to further approximate the centrifugal term during propagation[26] by writing

$$\hat{L}^2 \approx L_{\text{eff}}(L_{\text{eff}} + 1). \tag{17}$$

In this case, the results of the calculation will depend on the arbitrary choice of effective partial wave, L_{eff}. We do not make such approximations, but use Eq. (11), which is exact for the part of the centrifugal term that is diagonal in the body-fixed projection, K.

C. Contribution of bound states

In the discussion of the contribution of bound states, one should distinguish between the calculations with isotropic and anisotropic interactions. For an isotropic interaction, the spectral density is given by Eq. (8), where the translational profile, VG, has the following contributions involving bound states, in addition to the contribution from transitions between free states, Eq. (9). The contribution of bound-to-free transitions is given by[23]

$$\begin{aligned}
VG^{\text{bound-free}}_{l_1,l_2,l,\lambda}(\omega, T) = \hbar\lambda_0^3 \sum_{L,L'} [L, L'] \begin{pmatrix} L & \lambda & L' \\ 0 & 0 & 0 \end{pmatrix}^2 \\
\times \sum_n \exp\left(-\frac{E_{n,L}}{k_B T}\right) \\
\times |\langle E_{n,L}, L|D_{l_1,l_2,l,\lambda}|E_{n,L} + \hbar\omega, L'\rangle|^2,
\end{aligned} \tag{18}$$

where the sum is over all bound states n for partial wave L, and $|E_n + \hbar\omega, L'\rangle$ corresponds to a scattering state, i.e., $E_n + \hbar\omega > 0$. Contributions of free-to-bound transitions are determined from Eq. (18) by detailed balance and transitions between bound states contribute

$$\begin{aligned}
&VG^{\text{bound-bound}}_{l_1,l_2,l,\lambda}(\omega, T) \\
&\quad = \hbar\lambda_0^3 \sum_{L,L'} [L, L'] \begin{pmatrix} L & \lambda & L' \\ 0 & 0 & 0 \end{pmatrix}^2 \\
&\qquad \times \sum_{n,n'} \exp\left(-\frac{E_{n,L}}{k_B T}\right) |\langle E_{n,L}, L|D_{l_1,l_2,l,\lambda}|E_{n',L'}, L'\rangle|^2 \\
&\qquad \times \delta\left(E_{n',L'} - E_{n,L} - \hbar\omega\right).
\end{aligned} \tag{19}$$

The bound-state wave functions are determined using a sinc-function discrete variable representation (sinc-DVR).[27,28]

There are two aspects of the bound state contributions that should be discussed. First, the bound-to-bound contribution consists of a set of infinitely narrow absorption lines, since the bound complexes have infinite life time in the two-body theory. The δ-functions should be convolved with a line profile, for which we choose a normalized Gaussian of 0.12 cm^{-1} full width at half maximum. For all other contributions, the two body theory allows one to calculate the line-shape. The second aspect is one of interpretation. In the isotropic interaction approximation, any translational state can be combined with any rotational wave function. This means that the sum of the rotational and vibrational energies of bound states may be positive. On the anisotropic potential, such states of positive total energy are continuum states rather than bound states.

To compute the bound states on the anisotropic potential, we first determine a contracted radial basis as the lowest 50 eigenstates of a reference Hamiltonian with an isotropic reference potential

$$\begin{aligned} \hat{H}_0 &= -\frac{\hbar^2}{2\mu}\nabla_R^2 + V_{\rm ref}(R), \\ V_{\rm ref}(R) &= \lambda V_0(R - R_{\rm shift}) + \alpha R, \end{aligned} \tag{20}$$

where $V_0(R)$ is the isotropic part of the interaction.[29] The eigenstates of the reference Hamiltonian are determined using the sinc-DVR.[27,28] The shift $R_{\rm shift} = -1\ a_0$ allows the radial basis to accurately sample the repulsive region, which is otherwise only reached by states of very high energy. The scaling $\lambda = 3$ and the slope $\alpha = 3 \times 10^{-6}\ E_h/a_0$ improve the localization of the radial functions inside the potential well. These parameters were determined by variationally optimizing the energy of the bound states of the original Hamiltonian, Eq. (7).

The bound states of Hamiltonian Eq. (7) were then determined by diagonalizing the Hamiltonian matrix in a basis of direct products of the angular functions in Eq. (12) and the contracted radial functions described above. We calculate the bound states within the coupled-states approximation, discussed in Sec. III B. This leads to the eigenvalue problem of a sparse matrix, which is efficiently solved for the lowest eigenvalues using the Davidson algorithm.[30] Having converged the bound states, i.e., eigenstates with negative energy, the dipole coupling between these states is calculated. In order to calculate the coupling between bound and free states, we first compute the dipole operator acting on the bound state wave function. Then, we perform scattering calculations at energy $E = E_{\rm bound} + \hbar\omega$ and propagate the overlap between the free state and the product of dipole operator and bound state along with the free state wave function.[14]

IV. COMPUTATIONAL DETAILS

A. Spin statistics and molecular parameters

We assume that all four nitrogen nuclei are ^{14}N, which is the most abundant nitrogen isotope with a natural abundance of 99.6%. This nucleus is a boson with spin quantum number $I = 1$. For nitrogen molecule $X = A, B$, there are six symmetric nuclear spin wave functions corresponding to total nuclear spin $I_X = 0$ and 2, and there are three antisymmetric nuclear spin wave functions with $I_X = 1$. The total wave function should be symmetric with respect to the interchange of identical nuclei, which leads to the statistical weights for the rotational states $g_{N_X} = 6$ if N_X is even and $g_{N_X} = 3$ if N_X is odd. If we consider the colliding molecules to be distinguishable, the statistical weights for the rotational states of the complex are given by the product $g_{N_A} g_{N_B}$. For indistinguishable nitrogen molecules, the statistical weights depend on the permutation symmetry, ϵ, and their values are given in Table I.[31]

TABLE I. Nuclear spin statistical weights for all symmetries.

$(-1)^{N_A}$	$(-1)^{N_B}$	ϵ	$g^{\epsilon}_{N_A N_B}$
1	1	1	21
1	1	−1	15
−1	−1	1	6
−1	−1	−1	3
±1	∓1		18

The rotational energy levels of molecule $X = A, B$ are computed as

$$E_{{\rm rot},X} = BN_X(N_X + 1) - D[N_X(N_X + 1)]^2, \tag{21}$$

where N_X is the rotational quantum number, and the rotational and distortion constants are given by $B = 1.989\,581$ cm^{-1} and $D = 5.76 \times 10^{-6}$ cm^{-1}, respectively.[32]

B. Calculations with isotropic interactions

Calculations in the isotropic interaction approximation were performed as described in more detail in the companion paper.[14] The radial part of the scattering wave function is determined using the renormalized Numerov method.[33] This is calculated for each partial wave, L, on a discrete grid in the kinetic energy. The calculated dipole overlap integrals, $\langle E, L|D_{l_1,l_2,l,\lambda}|E', L'\rangle$, were obtained on discrete grids in the initial-state collision energy E and the energy difference $\hbar\omega = E' - E$, rather than in E and E', by spline interpolation of the logarithm of the square of the radial integral, as explained in Ref. 14. The integral over the initial state kinetic energy has been calculated using trapezoidal integration.

To converge the calculated spectrum to within 1%, we use partial waves up to $L_{\rm max} = 150$ and rotational quantum numbers up to $N_{\rm max} = 50$. The wave functions were calculated on a radial grid extending from 4 to 100 a_0, using the shortest local de Broglie wavelength divided by 10 as the step size, which amounts to a step size of approximately 0.03 a_0. The same step size is used in the sinc-DVR calculations for determining the bound state wave functions. The δ-function line-shape due to bound-to-bound transitions has been convolved with a Gaussian of 0.12 cm^{-1} width.

The isotropic potential supports a large number of shape resonances, some of which are very narrow. Consequently, the convergence of the calculation with respect to the number of grid points on a simple logarithmically spaced energy grid is not smooth. We use a tailored energy grid consisting of a logarithmically spaced grid with 200 steps on the interval from 0.1 K to 3000 K, augmented with 13 points per resonance. To

this end, we manually identified 39 resonances and estimated their widths, by inspecting the phase shifts, as explained in the Appendix.

C. Calculations with anisotropic interactions

Calculations in the coupled-states approximation were performed using a discrete grid in the photon frequency, ω/cm^{-1} = 30, 45, 60, 75, 90, 105, 120, and 180. For low energies, calculations were performed on a logarithmically spaced energy grid ranging from 0.1 K to 200 K in 165 steps. Additional calculations at higher energies were performed for E/K = 300, 400, 500, 700, 1000, 1400, and 2000. Convergence parameters for the basis set are given in Table II. Here, $J_{\max}$ is the highest total angular momentum included, whereas $N_{\max}$ refers to the truncation of the monomer angular momenta by the criterion

$$N_A(N_A+1)+N_B(N_B+1)\le N_{\max}(N_{\max}+1). \qquad (22)$$

The values of these parameters are chosen to ensure convergence of 1% or better.

Numerically exact close-coupling calculations were done for a single photon frequency, $\omega = 60\,\mathrm{cm}^{-1}$. These calculations were converged with the same convergence parameters as used in the coupled-states approximation as listed in Table II. The close-coupling calculations were performed only for low energies, using fewer energy grid points. A logarithmically spaced grid of 100 steps was used from 0.1 to 10 K with 4 additional points at energies 17.78, 31.62, 56.23, and 100 K.

For energies $E > 500$ K, the calculations are not performed for each value of J. Instead, J is increased in steps of 10, J = 0, 10, 20, . . ., and the results are interpolated by spline interpolation of the logarithm of the line strength followed by exponentiation. At the energy $E = 500$ K, calculations have been performed for all values of J, and at this energy, we confirm that the interpolation scheme is accurate to better than 1%. For higher energy, this interpolation scheme should become increasingly accurate.

Asymptotically closed channels, which are required only in the short range, are gradually removed from the calculations to save computational time.[14,34] We use an exponentially decaying energy criterion, which is chosen such that all channels are included for $R < 18\,a_0$ and all closed channels are removed for $R > 28\,a_0$.

We match the wave function to the scattering boundary conditions at $R = 100\,a_0$ for the lowest energies, which may be further than strictly necessary. For the energies $E = 1400$ K and $E = 2000$ K, we propagate only to $R = 30\,a_0$. We confirm at individual values of the quantum numbers J and K that this yields the same results to well within 1%.

The thermal average, Eq. (43) of our previous paper, has been performed as follows. We interpolate the logarithm of the line strength, as a function of the logarithm of the total energy, by spline interpolation. Then, we exponentiate the result, multiply with the Boltzmann factor, and perform the integral over the total energy using a trapezoidal integration rule. We estimate the accuracy of this approach by repeating the interpolating step with only half of the energy grid points. This reproduces the integral to an accuracy better than 5%.

Different convergence parameters are used for the sinc-DVR calculation of the bound state wave functions. The calculations were converged truncating the monomer rotational quantum numbers by the criterion Eq. (22) with $N_{\max} = 10$. All values of J and K for which bound states exist were included in the calculations. The highest total angular momentum for which bound states were found is $J = 30$. The radial coordinate was discretized by using a grid ranging from 4 to 100 a_0, with a step size of 0.05 a_0. A contracted radial basis was determined as the 50 lowest eigenstates of a reference Hamiltonian, as discussed in Sec. III C. The convergence criteria for the subsequent diagonalization of the Hamiltonian matrix using the Davidson algorithm are as follows: the search space is expanded until all bound states and the 10 lowest eigenstates of positive energy are converged, that is, until the norm of the residual of the tenth eigenstate of positive energy is smaller than 10^{-6}.[30] Again, the δ-function line-shape due to bound-to-bound transitions has been convolved with a Gaussian of 0.12 cm^{-1} width.

TABLE II. Convergence parameters of the coupled-states and close-coupling calculations.

Energy	$N_{\max}$	$J_{\max}$
0.1 K ≤ E ≤ 10 K	16	20
10 K ≤ E ≤ 100 K	16	45
100 K ≤ E ≤ 200 K	16	60
200 K < E ≤ 400 K	20	90
400 K < E ≤ 500 K	20	100
500 K < E ≤ 1000 K	26	150[a]
1000 K < E ≤ 2000 K	28	200[a]

[a]Interpolation as a function of J, according to the scheme discussed in the text.

V. RESULTS

A. Isotropic interaction approximation

Figure 1 shows the collision-induced absorption spectra at temperatures T = 78, 93, 126, 228.3, and 300 K. Crosses represent measurements in Refs. 7–10. Lines represent the

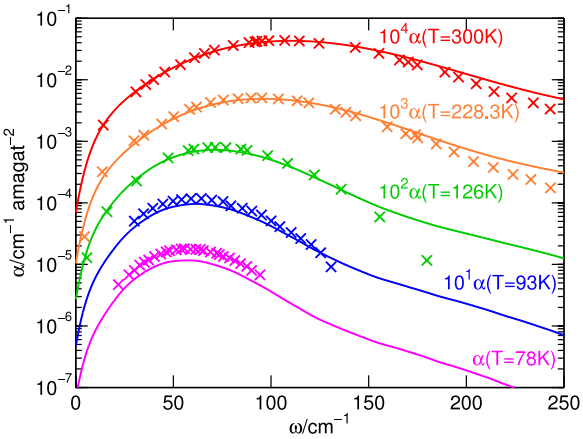

FIG. 1. Collision-induced absorption spectrum of N_2 for different temperatures. Lines mark theory with an isotropic interaction potential and the crosses represent measurements in Refs. 7–10. Spectra for successive temperatures have been shifted vertically, as indicated. Theoretical spectra have been smoothed to ensure clarity of this figure.

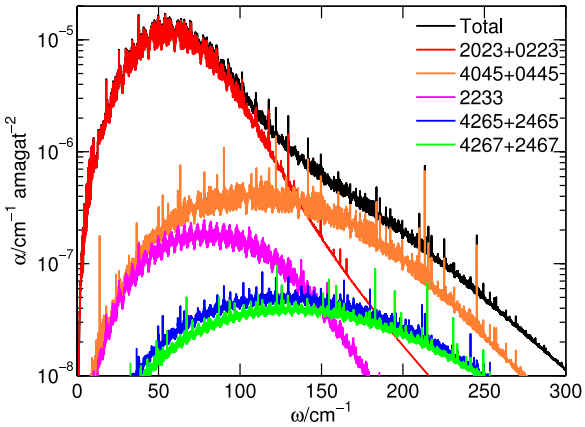

FIG. 2. Contribution of different spherical components of the dipole moment to the collision-induced absorption spectrum of N_2-N_2 at $T = 78$ K.

theoretical absorption spectra as calculated in the isotropic interaction approximation. The theoretical spectra include all binary contributions to the absorption: free-to-free, free-to-bound, bound-to-free, and bound-to-bound transitions. Reasonable agreement is obtained, although significant differences are observed mainly for low temperatures and in the far wing (high ω). For clarity of this figure, the theoretical spectra in this figure have been smoothed by convolution with a Gaussian of 11.7 cm^{-1} full width at half maximum. Sharp structures in the theoretical spectra do exist, and these are discussed below.

The contributions of the spherical components of the dipole moment to the spectrum at $T = 78$ K are shown in Fig. 2. The total absorption coefficient is shown by the black line, which shows sharp structures that were suppressed in Fig. 1. The dominant components are the l_1, l_2, l, $\lambda = 2, 0, 2, 3$ and 0, 2, 2, 3 terms. In first-order perturbation theory, these correspond to the quadrupole moment of one molecule which induces a dipole moment in the collision complex through the isotropic polarizability of the other molecule.[37] Higher terms in the spherical expansion contribute significantly in the far wing. This can be understood as these terms induce simultaneous transitions in both molecules and transitions with larger changes in the rotational angular momenta.

Figure 3 shows the translational profiles for free-to-free transitions at a temperature of $T = 78$ K as a function of the

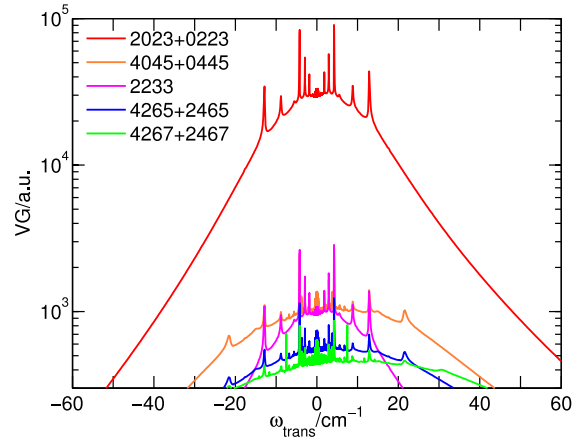

FIG. 3. Translational profiles due to free-to-free transitions for different spherical components of the dipole moment at $T = 78$ K.

angular frequency associated with the difference in kinetic energy through $\hbar\omega_{trans} = E'_{col} - E_{col}$. The red and the blue wings of the profile are related by detailed balance as $VG(-\omega) = \exp(-\hbar\omega/k_BT)\,VG(\omega)$. As discussed in Ref. 14, these profiles can be used to explain the shape of the absorption spectrum. At the lowest temperature, $T = 78$ K, the translational profiles are already broader than the typical rotational structure, which is determined by the rotational constant, $B_{rot} \approx 2$ cm^{-1}. Therefore, the rotational lines overlap in the spectrum (Fig. 1). We stress the difference with the H_2–H_2 system studied in the companion paper,[14] where the large rotational constant leads to a structured absorption spectrum with resolved rotational lines. The shift of the intensity to higher frequency with increasing temperature can be understood from the higher population of excited rotational states at elevated temperature.

The translational profiles in Fig. 3 show sharply peaked structures for low frequency, which occur repeatedly around each rotational transition in the absorption spectrum. These structures are due to the shape resonances supported by the isotropic potential. Resonant scattering wave functions have a large amplitude at short range, corresponding to a long life time of the collision complex, which leads to an enhanced dipole coupling. The sharp structure due to these resonances survives the thermal averaging in the computation of the translational profile only if ω equals the energy difference between two resonances of comparable width. For example, the structure at $\omega = 7.5$ cm^{-1} is due to transitions between resonant wave functions for $L = 18$, $E = 5.2$ cm^{-1} and $L' = 25$, $E' = 12.7$ cm^{-1}. Since the partial wave quantum number differs by 7, this transition contributes only to dipole components with $\lambda \geq 7$, and the peak near $\omega = 7.5$ cm^{-1} is visible only in the l_1, l_2, l, $\lambda = 4, 2, 6, 7 + 2, 4, 6, 7$ components in Fig. 3. If anisotropic interactions are taken into account, the shape resonances are expected to become less pronounced, especially for higher partial waves and energies. Therefore, the structure seen in the theoretical absorption spectrum, Fig. 2, must be considered an artifact of using the isotropic interaction approximation. We note that the shape resonances of the isotropic potential have not been discussed in previous calculations of the collision-induced absorption spectra of N_2–N_2 pairs.[6,35] We cannot be certain why this is the case, but it is possible that the energy grids employed in earlier work were too coarse to properly sample the narrow resonances.

The translational profiles for bound-to-free transitions at a temperature of $T = 78$ K are shown in Fig. 4. This figure also shows the contribution of the individual bound states for partial wave $L = 10$ to the translational profile. From a bound state at energy E_{bound}, the continuum cannot be reached below the threshold frequency given by $\hbar\omega_{thresh} = -E_{bound}$, and the bound-to-free contribution vanishes. The translational profile peaks just above threshold and falls off as ω is increased further, as the overlap between the involved states decreases as the energy gap increases. The contribution of weakly bound states is typically stronger as these states exhibit better overlap with continuum wave functions.

In Fig. 5, we compare the contributions of bound-bound, bound-free, and free-free transitions to the absorption at $T = 78$ K. Also shown in Fig. 5 are the absorption coefficients for free-to-free transitions and the contribution of bound states

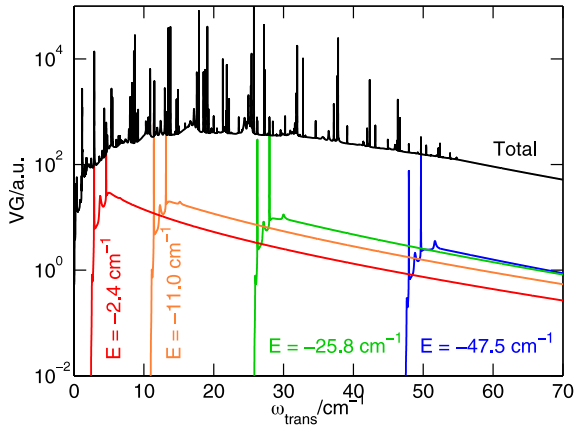

FIG. 4. Translation profile for bound-free transitions at $T = 78$ K. The black line marks the total translation profile, whereas the colored lines mark the contributions of the four bound states with $L = 10$ and bound-state energies as indicated.

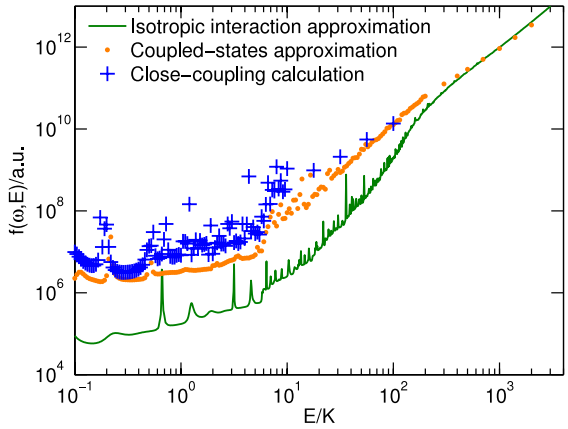

FIG. 6. Line strength as a function of the initial energy for a photon frequency $\omega = 60$ cm^{-1}. The solid line is obtained in the isotropic interaction approximation, dots represent results obtained in the coupled-states approximation, and pluses denote numerically exact close-coupling results.

from Ref. 6, as inferred from a computer code made available at Ref. 36. Both calculations were performed in the isotropic interaction approximation. The present calculations show much sharper features. In case of the bound-bound contributions, the width is somewhat arbitrary, but there is no obvious reason to smooth the lines beyond the natural width of the free-free and bound-free transitions. Again, we cannot be certain of the source of this discrepancy, but a possible explanation is the inaccurate sampling of shape resonances in earlier work.

B. Anisotropic interaction potential

In Fig. 6, we show the line strength for a fixed photon frequency, $\omega = 60\,\mathrm{cm}^{-1}$, as a function of the initial state energy. The line strength is defined as the total squared dipole moment,

$$f(\omega, E_{\mathrm{tot}}) = \sum_{i,f} g^{\epsilon}_{N_A N_B} |\langle i \| \hat{\boldsymbol{\mu}} \| f \rangle|^2, \tag{23}$$

where the sum over i is restricted to all states at energy E_{tot} and the sum over f is restricted to states of energy $E_{\mathrm{tot}} + \hbar\omega$. The line corresponds to the line strength in the isotropic interaction approximation, whereas the dots correspond to the coupled-states approximation with the full anisotropic potential energy surface. For low energy, $E \leq 100$ K, we also performed numerically exact close-coupling calculations, which are shown as crosses. Sharp scattering resonances occur at all three levels of theory, which are visible as sharp peaks in the line strength. The coupled-states approximation is reasonably close to the numerically exact results, the agreement improves for higher energies, and both methods agree well near $E = 100$ K. Deviations are observed mainly on the resonances, since these are very sensitive to approximating the centrifugal barrier by the coupled-states approximation.

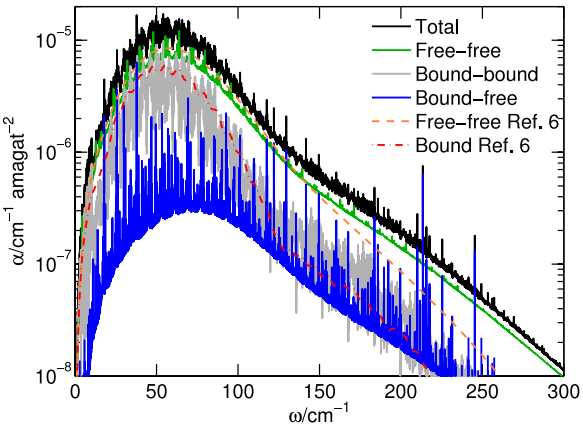

FIG. 5. Contributions of free-free, bound-free, and bound-bound transitions to the absorption spectrum at $T = 78$ K in the isotropic interaction approximation. The free-free transitions and bound state (bound-bound and bound-free) contributions from Ref. 6 are also shown as the orange dashed and red dashed-dotted lines, respectively.

In Fig. 7, we show the line strength for additional photon frequencies. For these frequencies, no close-coupling calculations have been performed. Scattering resonances occur only for total energies below ~20 cm^{-1} when the anisotropic interaction potential is used. This means that except at very low photon frequencies, the absorption spectrum will be a smooth function of ω. This contrasts with the sharp features observed above, for calculations in the isotropic potential approximation. In case of the isotropic potential, the narrow shape resonances occur for arbitrarily high total energies.

At low energies, $E \ll 100$ K, a difference of typically two orders of magnitude is observed between results obtained with the full anisotropic potential and results obtained using only the isotropic part, see Figs. 6 and 7. One contributor to the increase in the line strength is the closer approach of the colliding molecules on the anisotropic potential, because the induced dipole moment is much larger at short separation. By setting the dipole moment equal to zero for separations $R < 7\ a_0$, we find that only about 30% of the line strength at low energy stems from these short separations, which cannot be reached on the isotropic potential. This is a significant contribution to the dipole moment, but it is insufficient to explain an increase of the line strength at low energy by two orders of magnitude. Since the large increase of the line strength is not explained by the closer approach of the colliding molecules, we conclude that the dramatic effect of anisotropic interactions is due to angular localization of the scattering wave functions. The line strength is enhanced by localization near the T-shaped geometry, which

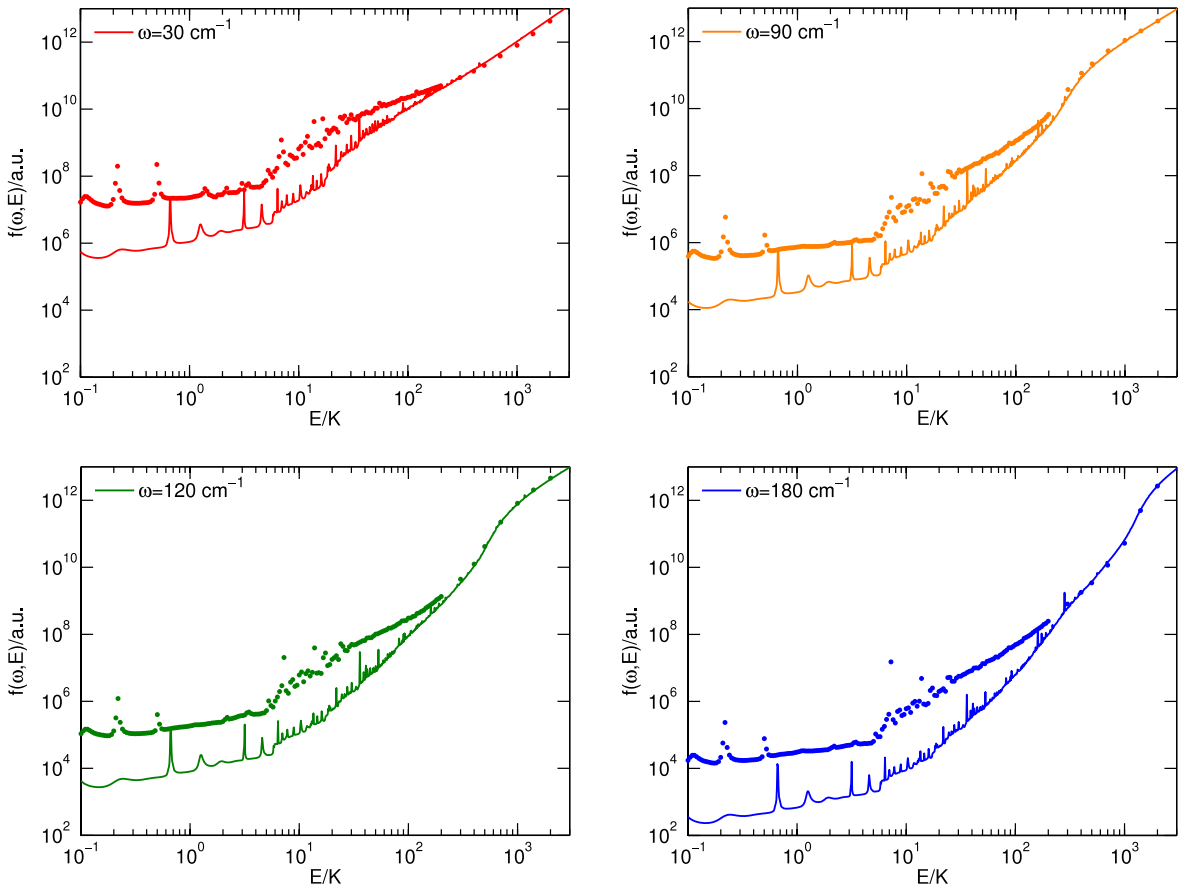

FIG. 7. Line strength as a function of energy for a fixed photon frequency as indicated. Lines represent results obtained in the isotropic interaction approximation, whereas dots are obtained in the coupled-states approximation.

corresponds to the minimum of the anisotropic potential energy surface. This T-shaped N_2–N_2 complex bears a relatively large dipole moment.

As seen in Fig. 7, the results of the isotropic interaction approximation approach the results of the more accurate coupled-states calculation for high energies, $E \gg 100$ K. This validates the isotropic interaction approximation as a high-temperature approximation to collision-induced spectra. This can be understood as the dynamics of energetic collisions are less sensitive to the details of the interaction potential. For high energy collisions, the molecules have insufficient time to adapt their orientations, whereas for slow collisions, the molecules may adiabatically follow orientations for which the interaction is attractive. Furthermore, a larger number of rotational states contributes to the total dipole moment at high energies, which may lead to some cancellation of errors in the thermal average of the calculation within the isotropic interaction approximation.

Figure 8 shows the different binary contributions to the absorption spectrum at $T = 78$ K in the coupled-states approximation, including the full anisotropic potential. The dots, the crosses, and the dotted line represent the free-free, bound-free, and bound-bound contributions, respectively. For comparison, the smoothed total absorption spectrum in the isotropic interaction approximation is included as the solid line. The contribution of bound states is significant, albeit not as strong as in the isotropic interaction approximation. The reason is explained in Sec. III C: in the isotropic interaction approximation, bound states of positive total energy exist, as bound translational states can be combined with rotational state of arbitrarily high energy. In the anisotropic case, such states of positive energy become part of the continuum. Since bound states only occur for negative total energy when anisotropic interactions are considered, the bound-to-bound contribution is naturally limited by the well-depth of the potential. Also apparent is the smoothness of the spectrum when anisotropic interactions

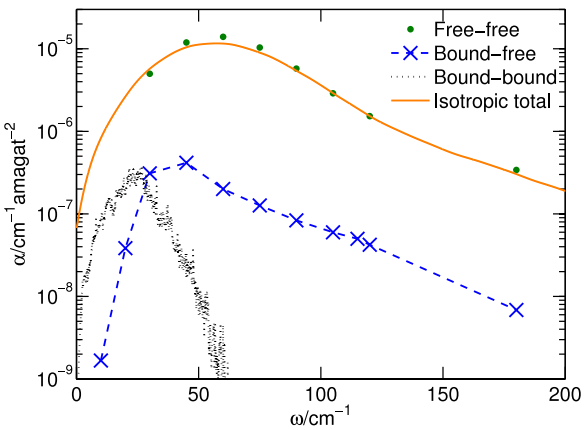

FIG. 8. Different contributions to the collision-induced spectrum at temperature $T = 78$ K using the full anisotropic interaction potential in the coupled-states approximation. For comparison, the total absorption in the isotropic interaction approximation is included. This contribution has been smoothed for clarity of the figure.

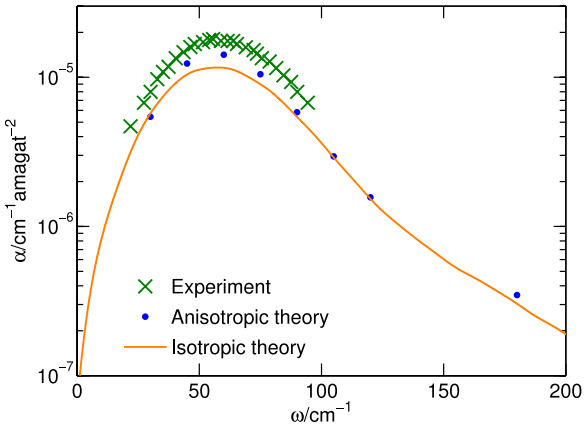

FIG. 9. Collision-induced spectrum at temperature $T = 78$ K. Crosses represent measurements in Ref. 10, the line represents theoretical results in the isotropic interaction approximation, and dots are theoretical results using the full anisotropic interaction potential in the coupled-states approximation. The result in the isotropic interaction approximation has been smoothed for clarity of the figure.

are included, as opposed to the unphysically sharp features observed for calculations in the isotropic interaction approximation. Even the bound-to-bound contribution is reasonably smooth with the narrow artificial broadening of the δ-functions by only 0.12 cm^{-1}.

Figure 9 shows the collision-induced rotation-translation spectrum of N_2–N_2 at a temperature of $T = 78$ K, where the crosses represent the experimental data by Ref. 10, the dots are theoretical results using the full anisotropic interaction potential in the coupled-states approximation, and the solid line shows the spectrum obtained in the isotropic interaction approximation. For clarity of this figure, the spectrum obtained in the isotropic interaction approximation has been smoothed by convolution with a Gaussian of 11.7 cm^{-1} full width at half maximum. Considering anisotropic interactions increases the overall intensity of the collision-induced rotation-translation band of N_2–N_2. This is consistent with the findings of Ref. 13, and brings the calculated spectra into closer agreement with experimental data near the band maximum.[10] The difference between theory and experimental data for $T = 78$ K is reduced from 34% to 19%, which is still larger than the estimated 5% experimental error. The remaining difference is attributed to systematic errors in the experiment, as discussed in Ref. 10, and inaccuracy of the dipole coefficients on the theoretical side, as discussed below. Absorption coefficients for temperatures between 50 K and 300 K can be found in Table III.

Inclusion of anisotropic interactions does not improve the far wing of the spectrum, which is systematically overestimated by our calculations, see higher temperatures in Fig. 1. A possible explanation for the difference between experiment and theory is the uncertainty of the measurements, as the experimental error is largest in the far wing, where the absorption nearly vanishes. On the theoretical side, we expect that the largest errors come from the determination of the coefficients in the spherical harmonic expansion of the dipole moment surface in Eq. (2). Inaccuracy in the higher spherical-harmonic coefficients affects only the far wings of the spectra, as can be seen from Fig. 2. Test calculations with additional field strengths, and comparisons of the results obtained with aug-cc-pVQZ and the larger aug-cc-pV5Z basis sets, both at CCSD(T) level, suggest that the values of the potential energy and dipole moment for the individual geometrical configurations of the N_2–N_2 pair are relatively well converged. However, uncertainties remain in the coefficients for the spherical harmonic expansion, obtained by fitting to the *ab initio* points. To reduce these uncertainties, results from a large number of additional *ab initio* calculations at suitably chosen geometries are needed. This will permit the inclusion of more terms in the spherical harmonic expansion, as well as more accurate determination of the coefficients already included.

TABLE III. Tabulated absorption coefficients for temperatures between 50 K and 300 K and a range of frequencies. The absorption was calculated using the full anisotropic interaction potential in the coupled-states approximation, including contributions of bound states. Absorption coefficients are given in units of cm^{-1} amagat^{-2}, and numbers in parentheses denote powers of ten.

	ω/cm^{-1}							
T/K	30	45	60	75	90	105	120	180
50	1.52 (−5)	2.79 (−5)	2.24 (−5)	1.14 (−5)	5.09 (−6)	2.65 (−6)	1.58 (−6)	3.74 (−7)
55	1.20 (−5)	2.34 (−5)	2.04 (−5)	1.12 (−5)	5.11 (−6)	2.58 (−6)	1.49 (−6)	3.60 (−7)
60	9.79 (−6)	1.99 (−5)	1.87 (−5)	1.11 (−5)	5.23 (−6)	2.58 (−6)	1.45 (−6)	3.52 (−7)
70	6.90 (−6)	1.51 (−5)	1.60 (−5)	1.08 (−5)	5.56 (−6)	2.74 (−6)	1.48 (−6)	3.46 (−7)
80	5.15 (−6)	1.18 (−5)	1.38 (−5)	1.04 (−5)	5.90 (−6)	3.01 (−6)	1.60 (−6)	3.48 (−7)
90	4.02 (−6)	9.51 (−6)	1.20 (−5)	9.94 (−6)	6.16 (−6)	3.31 (−6)	1.78 (−6)	3.55 (−7)
100	3.23 (−6)	7.83 (−6)	1.05 (−5)	9.44 (−6)	6.35 (−6)	3.61 (−6)	1.99 (−6)	3.66 (−7)
125	2.08 (−6)	5.18 (−6)	7.80 (−6)	8.16 (−6)	6.47 (−6)	4.24 (−6)	2.58 (−6)	4.15 (−7)
150	1.47 (−6)	3.70 (−6)	6.01 (−6)	6.99 (−6)	6.28 (−6)	4.63 (−6)	3.12 (−6)	5.04 (−7)
175	1.12 (−6)	2.80 (−6)	4.76 (−6)	6.00 (−6)	5.91 (−6)	4.80 (−6)	3.53 (−6)	6.38 (−7)
200	8.89 (−7)	2.20 (−6)	3.89 (−6)	5.18 (−6)	5.48 (−6)	4.81 (−6)	3.81 (−6)	8.11 (−7)
225	7.33 (−7)	1.79 (−6)	3.24 (−6)	4.50 (−6)	5.05 (−6)	4.72 (−6)	3.98 (−6)	1.01 (−6)
250	6.21 (−7)	1.49 (−6)	2.74 (−6)	3.94 (−6)	4.63 (−6)	4.57 (−6)	4.06 (−6)	1.21 (−6)
275	5.38 (−7)	1.27 (−6)	2.34 (−6)	3.48 (−6)	4.25 (−6)	4.38 (−6)	4.07 (−6)	1.41 (−6)
300	4.74 (−7)	1.10 (−6)	2.05 (−6)	3.10 (−6)	3.90 (−6)	4.18 (−6)	4.03 (−6)	1.59 (−6)

VI. CONCLUSIONS

We have presented a theoretical study of the collision-induced absorption spectra of N_2–N_2. In contrast with earlier quantum mechanical studies of these spectra, we use *ab initio* dipole moment and potential energy surfaces free of empirically adjusted parameters and we use the full anisotropic interaction potential energy surface. Angular localization of the scattering wave function due to anisotropic interactions is seen to increase the line strength at low energies by two orders of magnitude. Good agreement with experimental data is obtained and the agreement improves upon inclusion of anisotropic interactions. The effect of anisotropic interactions decreases at higher energy, which validates the isotropic interaction approximation as a high-temperature ($T > 100$ K for N_2–N_2) approximation for calculating collision-induced spectra. This is consistent with the classical simulations reported in Ref. 13. The unambiguous identification of quantum effects would require quantum mechanical calculations and classical simulations using the same potential energy and dipole moment surfaces.

ACKNOWLEDGMENTS

The authors gratefully acknowledge the computer and communication department (CNCZ) of the science faculty of the Radboud University Nijmegen for the computer resources made available as well as for technical support. This work has been supported in part by Grant No. 0708496 from the National Science Foundation (U.S.).

APPENDIX: SHAPE RESONANCES ON THE ISOTROPIC POTENTIAL

The isotropic potential supports a large number of shape resonances, some of which are very narrow. In order to construct an energy grid that properly samples these resonances, we manually identified the positions and widths of 39 resonances by inspecting the phase shifts, defined through the S-matrix by $S = \exp(i2\delta)$. The phase shift is typically a smooth function of the collision energy, but rapidly jumps by π on resonance. In Fig. 10, we show the phase shifts for a number of partial waves.

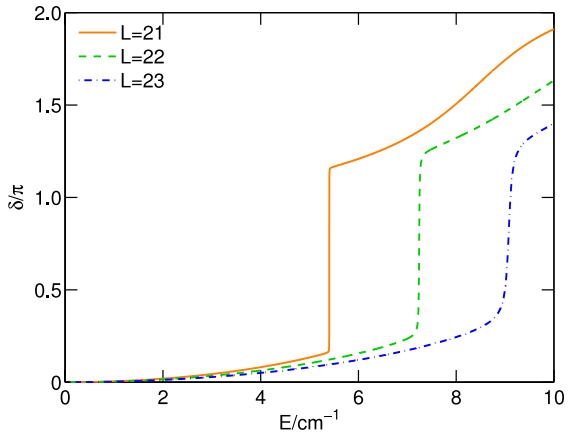

FIG. 10. The phase shift as a function of the collision energy for shape resonances on the isotropic potential.

[1]P. von Paris, J. Grenfell, H. Rauer, and J. Stock, Planet. Space Sci. **82**, 149 (2013).
[2]C. M. Anderson and R. E. Samuelson, Icarus **212**, 762 (2011).
[3]J.-M. Hartmann, C. Boulet, and D. Robert, *Collisional Effects on Molecular Spectra* (Elsevier, 2008).
[4]Q. Ma and R. H. Tipping, J. Chem. Phys. **112**, 574 (2000).
[5]M. Höpfner, M. Milz, S. Buehler, J. Orphal, and G. Stiller, Geophys. Res. Lett. **39**, 10706, doi: 10.1029/2012gl051409 (2012).
[6]A. Borysow and L. Frommhold, Astrophys. J. **311**, 1043 (1986).
[7]N. W. B. Stone, L. A. A. Read, A. Anderson, I. R. Dagg, and W. Smith, Can. J. Phys. **62**, 338 (1984).
[8]I. R. Dagg, A. Anderson, S. Yan, W. Smith, and L. A. A. Read, Can. J. Phys. **63**, 625 (1985).
[9]P. Dore and A. Filabozzi, Can. J. Phys. **65**, 90 (1987).
[10]E. H. Wishnow, H. P. Gush, and I. Ozier, J. Chem. Phys. **104**, 3511 (1996).
[11]J. Boissoles, R. Tipping, and C. Boulet, J. Quant. Spectrosc. Radiat. Transfer **51**, 615 (1994).
[12]J. Boissoles, C. Boulet, R. Tipping, A. Brown, and Q. Ma, J. Quant. Spectrosc. Radiat. Transfer **82**, 505 (2003).
[13]B. Bussery-Honvault and J.-M. Hartmann, J. Chem. Phys. **140**, 054309 (2014).
[14]T. Karman, A. van der Avoird, and G. C. Groenenboom, J. Chem. Phys. **142**, 084305 (2015).
[15]M. Gustafsson, L. Frommhold, and W. Meyer, J. Chem. Phys. **113**, 3641 (2000).
[16]M. Gustafsson, L. Frommhold, D. Bailly, J.-P. Bouanich, and C. Brodbeck, J. Chem. Phys. **119**, 12264 (2003).
[17]E. Miliordos and K. L. C. Hunt, "Theoretical calculation of the second pressure, acoustic, Joule-Thomson, refractivity and dielectric virial coefficients of molecular hydrogen," J. Chem. Phys. (submitted).
[18]S. F. Boys and F. Bernardi, Mol. Phys. **19**, 553 (1970).
[19]See supplementary material at http://dx.doi.org/10.1063/1.4907917 for *ab initio* points and expansion coefficients of the potential energy and dipole moment surfaces of N_2–N_2.
[20]K. T. Tang and J. P. Toennies, J. Chem. Phys. **80**, 3726 (1984).
[21]T.-S. Ho and H. Rabitz, J. Chem. Phys. **104**, 2584 (1996).
[22]G. Birnbaum, S.-I. Chu, A. Dalgarno, L. Frommhold, and E. L. Wright, Phys. Rev. A **29**, 595 (1984).
[23]W. Meyer, L. Frommhold, and G. Birnbaum, Phys. Rev. A **39**, 2434 (1989).
[24]A. van der Avoird, P. E. S. Wormer, and R. Moszynski, Chem. Rev. **94**, 1931 (1994).
[25]J. M. Hutson and S. Green, Molscat computer code, version 14, distributed by Collaborative Computational Project No. 6 of the Engineering and Physical Sciences Research Council, UK, 1994.
[26]P. McGuire and D. J. Kouri, J. Chem. Phys. **60**, 2488 (1974).
[27]D. T. Colbert and W. H. Miller, J. Chem. Phys. **96**, 1982 (1992).
[28]G. C. Groenenboom and D. T. Colbert, J. Chem. Phys. **99**, 9681 (1993).
[29]H. Cybulski, R. V. Krems, H. R. Sadeghpour, A. Dalgarno, J. Kłos, G. C. Groenenboom, A. van der Avoird, D. Zgid, and G. Chałasiński, J. Chem. Phys. **122**, 094307 (2005).
[30]E. R. Davidson, J. Comput. Phys. **17**, 87 (1975).
[31]P. R. Bunker and P. Jensen, *Molecular Symmetry and Spectroscopy*, 2nd ed. (NRC Research Press, Ottawa, 1998).
[32]J. Bendtsen, J. Raman Spectrosc. **2**, 133 (1974).
[33]B. R. Johnson, NRCC Proc. **5**, 86 (1979).
[34]R. Martinazzo, E. Bodo, and F. Gianturco, Comput. Phys. Commun. **151**, 187 (2003).
[35]M. El-Kader, S. Mostafa, T. Bancewicz, and G. Maroulis, Chem. Phys. **440**, 127 (2014).
[36]A. Borysow and L. Frommhold, Fortran code, http://www.astro.ku.dk/~aborysow/programs/.
[37]J. E. Bohr and K. L. C. Hunt, J. Chem. Phys. **87**, 3821 (1987).